Springer

KSME

Journal of Mechanical Science and Technology 31 (7) (2017) 3305~3315
www.springerlink.com/content/1738-494x(Print)/1976-3824(Online)
DOI 10.1007/s12206-017-0621-3

Image post-processed approaches for cavitating flow in orifice plate †

Yong Wang[1], Suguo Zhuang[2], Houlin Liu[1], Zhenjiang Zhao[3], Matevž Dular[4] and Jian Wang[3,*]

[1]*Research Center of Fluid Machinery Engineering and Technology, Jiangsu University, Zhenjiang 212013, Jiangsu, China*
[2]*Xi'an Aerospace Propulsion Institute, Xi an 710100, Shanxi, China*
[3]*School of Shipping and Mechatronic Engineering, Taizhou University, Taizhou 225300, China*
[4]*Laboratory for Water and Turbine Machines, Faculty of Mechanical Engineering, University of Ljubljana, Askerceva 6, 1000 Ljubljana, Slovenia*

(Manuscript Received December 4, 2016; Revised February 3, 2017; Accepted March 7, 2017)

Abstract

A comprehensive investigation on cavitating flow and cavitation-induced erosion was performed experimentally in an orifice plate system. Three image post-processed approaches were applied to analyze the test data, in order to obtain the cavitation characteristics. The cavitating flow pattern was studied by high speed images. In one cavitation developing period, there could be three distinct cavitation clouds, whereas the second one is not fully developed. The first image post-processing approach was applied to obtain the mean value and standard deviation distribution, which indicate the erosion area may cover almost all the cavitation developing route and the most vulnerable erosion area locates near the cavitation collapse site. It is coincides with the erosion tests analyzed through the pit-count algorithm approach. The cavitation circulation frequency was invested via PSD analysis approach. It shows that the frequency linearly decreasing with decreasing cavitation number. Additionally, the cavitation intensity effect on cavitation erosion was quantitatively studied based. It is found that the damages are strongly enhanced when increasing the flow velocity. Moreover, the growth rate of eroded pits number is actually stepwise instead of linear (similar to our previous work in a venturi tube), which supports the idea that the cloud cavitation collapse is the primary reason for erosion. The present approaches applied here shows good potential ability of investigating cavitating flows and can be utilized for other apparatus.

Keywords: Cavitating flow; Cavitation erosion; Visualization; Collapse; Orifice plate

1. Introduction

Cavitation is defined as bubbles generation. It happens where the local pressure is below the liquid saturation pressure, and then the bubbles collapse when they are convected downstream, because of pressure recovery. If the collapse occurs in the vicinity of solid wall, the shock wave or micro jet generated during this process would erode the surface of the rigid boundary. As the energy impacting on the surface exceeds the material's fatigue strength, then erosion happens. Such damage pattern is found almost in every hydrodynamic machines, like vessels, propellers, pumps and so on, resulting in enormous economic lose [1-9].

Remarkable attempts have been made to clarify the physical mechanism of cavitation erosion, since last century in 1917 Rayleigh discussed about the issue of cavitation erosion on ship propellers [10]. The intensity of the shock wave emitted by bubbles collapse is one of the most important factors resulting in cavitation erosion, which could reach several GPa [11, 12]. Various measurement approaches are applied to obtain the impact load on solid surface. But it seems like that different approaches might get different results. Franc et al. [13] tested the cavitation generated by two parallel circular plates with a straight nozzle on one of them in the center, and the other one was placed 2.5 mm away as the eroded sample. A maximum impact load of 500 N was measured via a conventional pressure transducer as the cavity velocity ranges from 45 m/s to 90 m/s. However, Carnelli et al. [14] only got an order of 20 N impact load on a same test system by using the spherical nanoindentation measurement. Also, Hattori et al. [15] obtained similar results (a maximum impact load of 20 N) at flow velocity up to 184 m/s by following the standard ASTM G124-95. Furthermore, Soyama et al. [16] employed the Poly vinylidene fluoride (PVDF) to measure the impact load in a cavitating jet device. It turned out to be up to 200 N when the jet velocity at the nozzle outlet ranges from 126 m/s to 155 m/s. The discrepancy between these tests was significant. One of the reasons lies in that the size of the pressure transducers adopted in these works are still larger than the tiny bubbles, although they are "micro". The measured impact load may be caused by several bubbles collapse. And the lower

*Corresponding author. Tel.: +86 13775530081
E-mail address: arieskin@126.com
† Recommended by Associate Editor Sangyoup Lee

sampling frequency of the pressure transducer, compared with the fast progress of collapse, could also influence the test result.

Another prevalent measurement is the pitting test, first proposed by Knapp in the 1950s [17, 18]. By exposing the solid material to a cavitating flow, it is used as a transducer during the erosion incubation period, which means the material only suffers plastic deformation without mass loss. In this way, one can obtain the distribution of pits and even the number and area, but such erosion experiments still require a long exposure time [19-23]. Hutli et al. [20] tested the cavitation erosion process by exposing the copper samples to a high speed submerged cavitating jet for 30 min. Rijsbergen et al. [23] tested cavitating flow around a 2D NACA hydrofoil, aiming at studying the sheet cavitation collapse behavior and related erosion mechanism. The detailed cavitation evolution structures were captured from side and top views by two high speed cameras. And the cavitation erosion was measured by oil painting method for 1 hour. Such long testing time makes it difficult to investigate the relationship between cavitation structures and erosion. A common way to solve this issue is the utilization of softer material as the transducer [24, 25]. Recently, our previous work applied a thin aluminum foil attached on the solid surface as an erosion sensor. The tests only lasted few seconds to minutes, which enabled us to record the cavitation erosion progress and the cavitation evolution synchronously by high speed camera [26-28]. The results presented a strong demonstration that the cloud cavity separation and collapse are responsible for the damage.

In the meantime, great effort has been made on the prediction of cavitation erosion, based on various mechanisms [29-34]. And most of them were conducted by CFD method. A recent study performed by Gavaises et al. [35] predicted the cavitation area in an axisymmetric geometry (similar to the current work) via both visualization and CFD approaches, in order to correlate the eroded location with the location of cavitation development. The simulation results had great agreement with the visualizations.

In the present study, we performed jet flow cavitation tests through two adjacent parallel plates with a nozzle tube—orifice plate. Aiming at providing insight into the details of the correlation between cloud cavitation collapse and cavitation-induced erosion, and establishing fully experimental methods for investigating different cavitating devices, three image post-processing approaches were employed to analyze the cavitation characteristics. The prediction results were validated by cavitation erosion tests.

2. Experimental setup

All the experiments were conducted in a cavitation loop test platform in the Laboratory for Water and Turbine Machines, University of Ljubljana. As seen in Fig. 1, the entire closed test system was driven by a loop pump, a upstream tank which can be used for water heating, a downstream tank which is

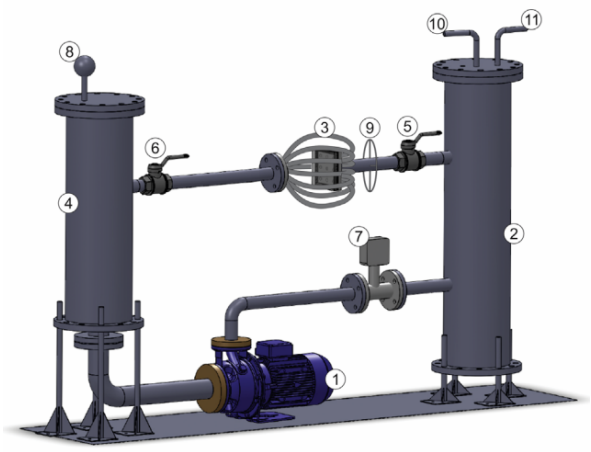

① Loop pump, ② Downstream tank, ③ Orifice plates, ④ Upstream tank, ⑤, ⑥ Valves, ⑦ Electromagnetic flow meter, ⑧ Heater, ⑨ Pressure transducer, ⑩ Compressor, ⑪ Vacuum pump

Fig. 1. Test rig.

connected with a compressor and a vacuum pump for controlling the system pressure, a test section composed of two parallel plates, an electromagnetic flow meter, ABB WaterMaster V with a measurement uncertainty of 2 % and two pressure transducers, ABB 266AST with ±0.04 % measurement uncertainty. Hence, the measurement uncertainties due to instruments was estimated less than 3 %. The detailed test rig facilities can be referred in Ref. [28].

In the attempt of obtaining the full cavitation erosion data from the very beginning of the cavitation being generated, two valves are mounted upstream and downstream from the test section, far enough for avoiding disturbance. To assure the test repeatability, the dissolved gases were measured by the Van-Slyke method [36] after running the test rig for 30 min at a low pressure, since the dissolved gases have significant influence on cavitation. In the presented work, the gas content of 15 mg/L in water was maintained.

The test section was manufactured by Plexiglas for visualization. As mentioned above, it consists of two square parallel plates with a dimension of 150 mm×150 mm. The flow comes through a nozzle tube at the center of the upstream plate, where the cavitation generates at the throat. And then it moves downstream through four symmetrical outlet holes on the periphery. The downstream plate is used as the eroded target. The distance between two plates is controlled by a washer with a thickness of 3 mm. The profile of the test section is illustrated in Fig. 2, as well as the real model.

The high speed camera, Fastec Imaging HiSpec4 2G, was placed in the front of the downstream plate. It has a maximum resolution of 3Mpixel with a sampling frequency of 523 fps. The cavitation evolution under different cavitation number in the first place. The cavitation number is a dimensionless parameter defined as: $\sigma = (p_\infty - p_v)/0.5\rho v^2$. Here p_∞ stands for the reference pressure, measured 200 mm upstream from the test section. p_v = 3170 Pa is the water saturation pressure, v de-

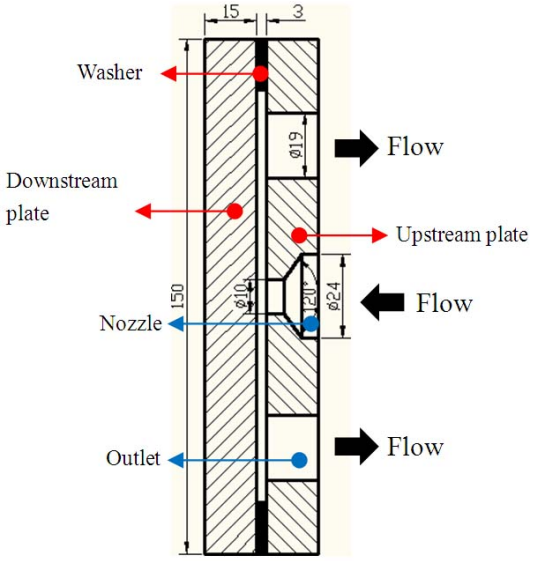

(a)

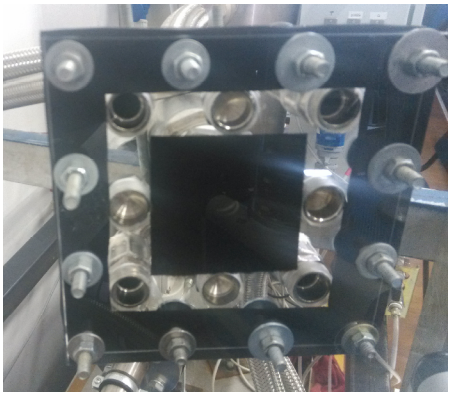

(b)

Fig. 2. (a) Profile of the orifice plate; (b) the real model.

notes the velocity at the nozzle throat and ρ = 998.2 kg/m^3 means the water density.

During the cavitation erosion tests, the pump was firstly operated at a low frequency to get the water circulating in the system at a low velocity without any cavitation. Then, the desired operating condition was set by closing the upstream valve and switched the pump operating frequency. At the end, the desired operating condition was achieved by opening the upstream valve rapidly. The cavitation damages were measured by a 10 μm thick aluminum foil attaching on the downstream plate. The eroded progress was also recorded by high speed camera, since the exposure time only lasts for 5 min. The whole test section is symmetrical, so the foil only covers part of the surface, as shown in Fig. 3.

3. Results and discussions

Fig. 4 shows the instantaneous cavitation structures under various cavitation numbers. These successive images were recorded by high speed camera at a shooting frequency of

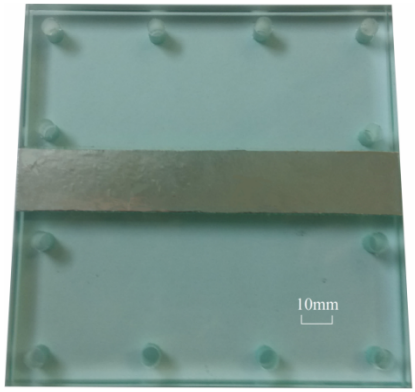

Fig. 3. Aluminum foil attached downstream plate.

2773 fps for 2 min.

As seen, the cavitation structure is annular, and the size increases with the decreasing cavitation number. For σ = 3.36, the length reaches 26.9 mm (from the cavitation inception point to collapse point), while it is only 6.1 mm at σ = 5.15. Also, because the distance between two plates is only 3 mm, we can note that the generated cloud cavitation is composed of numerous tiny bubble clusters.

For predicting the eroded areas, the successive images of the cavitation structure were post-processed by calculating the standard deviation valve. Each image is treated as matrix, within which every each element indicates one pixel. So the image can be expressed as:

$$Iamge(n) = \begin{pmatrix} A(1,1,n) & \cdots & A(i,1,n) \\ A(1,2,n) & \cdots & A(i,2,n) \\ \vdots & \ddots & \vdots \\ A(1,j,n) & \cdots & A(i,j,n) \end{pmatrix} \quad (1)$$

where n stands for the number of the images, $A(i,j,n)$ denotes the element, $A(i,j,n) \in \{0,1,...255\}$ (0 for black pixel and 225 for while pixel, 256 levels in total). On the premise of this, the image mean value and standard deviation are defined as:

$$\mu(i,j) = \frac{1}{N}\sum_{n=1}^{N} A(i,j,n) \quad (2)$$

$$\zeta(i,j) = \sqrt{\frac{1}{N-1}\sum_{n=1}^{N}[A(i,j,n) - \mu(i,j)]^2} \quad (3)$$

Here $\mu(i,j)$ represents the mean value of the image. More details concerning to the applied post-processing approach can be found in Ref. [37].

Fig. 5 presents the mean value and standard deviation distribution under various cavitation numbers. From which, we can identify the cavitation covering area via the mean value distribution, and predict the potential eroded area through the standard deviation distribution.

One can notice that the size of the mean value and standard deviation distributions are almost identical with each other.

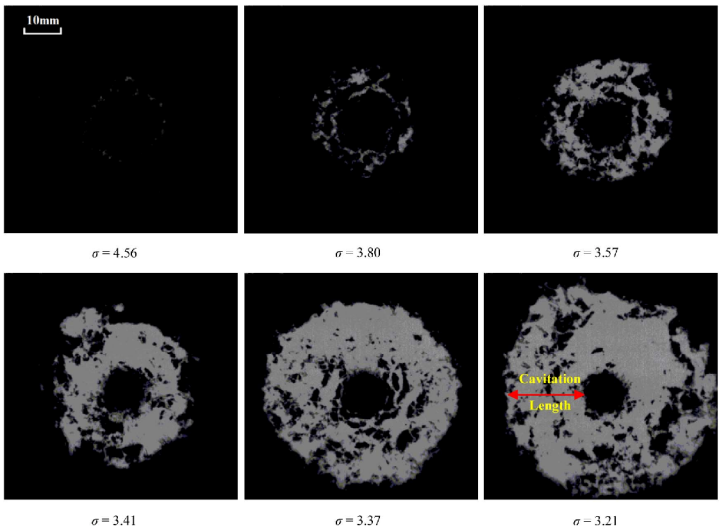

Fig. 4. Cavitation structure under various cavitation numbers.

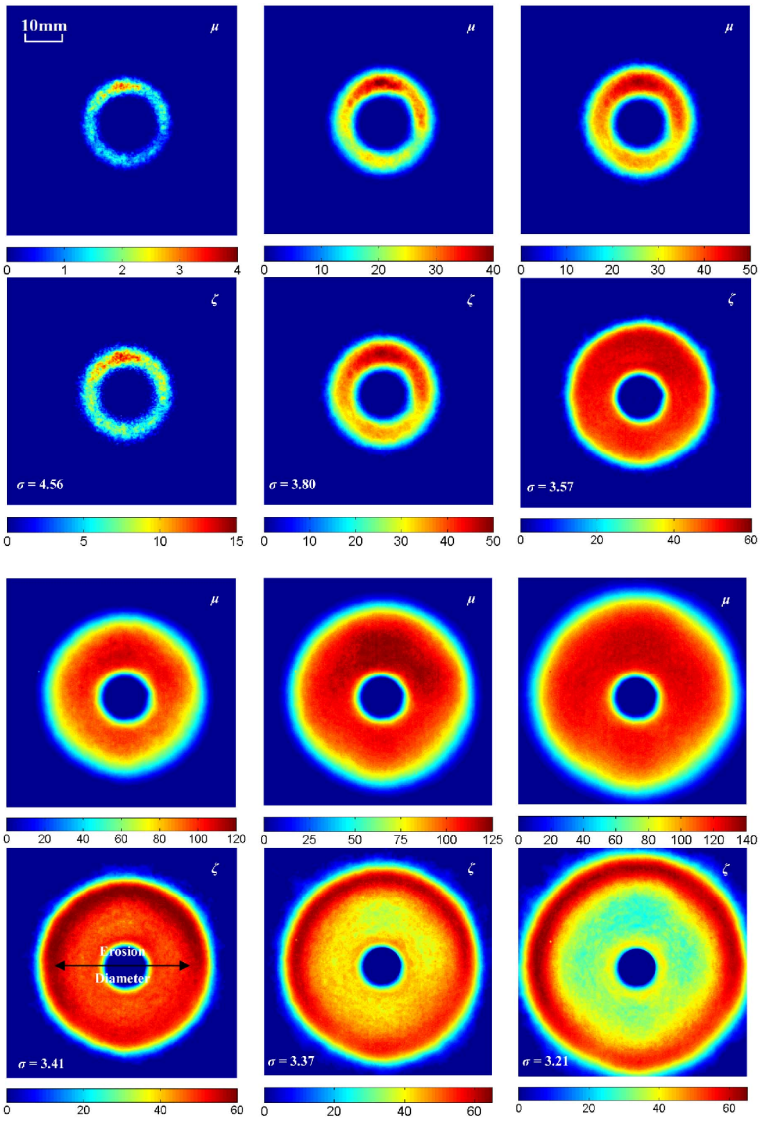

Fig. 5. Mean value (upper) and standard deviation distribution (below) under various cavitation numbers.

However, the contours are not that analogous when the cavitation number drops below 3.41. The standard deviation indicates that the most potential erosion region locates on the periphery with highest deviation value, while the most covered cavitation region given by the mean value lie in the middle of the contour (The scales of the standard deviation and mean value are used for better image contrast to identify the cavity covered region and potential erosion region).

When the cavitation number goes above 3.57, the distributions are nearly the same. The reason is that as the cavitation number decreases, the cavitation evolution process becomes more distinct and regular. As a result, the likely eroded area concentrates at the sites where collapse occurs, making it prone to be damaged by emitted shock wave or jet flow. Whereas the cavitation evolution is a little irregular as the cavitation number is higher. Besides, one may find that the distribution is not strict symmetrical. We reckon that it is probably caused by the uneven screw intension.

In order to obtain better resolution of the cavitation evolution progress, much higher shooting frequency was set by narrowing the observation area (40820 fps in this case), as framed in Fig. 6 by red solid enclosing-square. Here we selected the operating condition of $\sigma = 3.41$ for analyzing.

Fig. 7(a) shows one entire cavitation period, together with

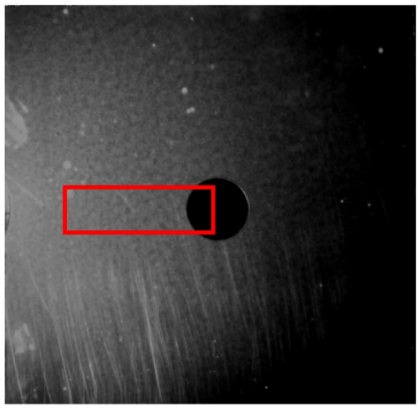

Fig. 6. Narrowed observation area.

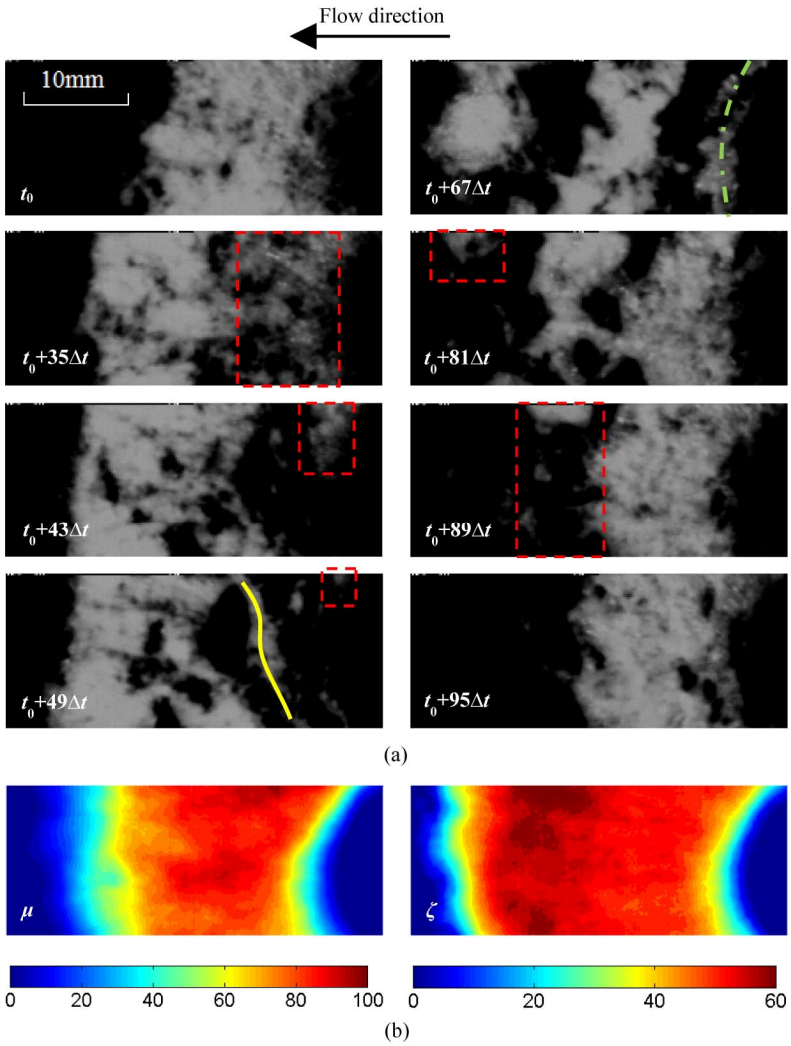

Fig. 7. Cavitation evolution (a) combined with the mean value (left) and standard deviation (right); (b) at $\sigma = 3.41$.

the mean value and standard deviation distribution, where Δt = 0.0245 ms. The flow direction is from right to left. It should be noted that the time intervals between each image are not the same, for displaying the critical moments during the evolution.

One can see that when $t = t_0$, the cavitation is attaching on the solid surface and slowly growing towards downstream. $35\Delta t$ later, it starts shedding off and separates into two parts. The detached part moves to downstream along with the main flow, while the front part stays still and then gradually collapses, which is highlighted by red dash lines at $t_0+35\Delta t$ and $t_0+43\Delta t$. It finally disappears around $t_0+49\Delta t$. In the meantime, a second cavitation cluster is generated after the one detached in the first place, marked by yellow solid line. However, it should be noticed that it is not another round of cavitation inception, because it turns out shedding off soon without enough developing. One can recognize this process when the time comes to $t_0+67\Delta t$, only $18\Delta t$ later. The second cavitation cluster streams after the first cloud directly. Shortly after, the real periodic cavitation inception appears, marked by green dash-dot line. Consequently, there are three distinct cavitation clusters at the same time: The first detached cavitation cloud, which is already shrinking currently, the second followed cavitation cluster and the third newly incepted attaching cavitation, which will keep growing from $t_0+67\Delta t$ till the status like $t = t_0+35\Delta t$. Afterwards, the first and second cavitation clusters, encircled by red dash line at $t = t_0+81\Delta t$ and $t = t_0+89\Delta t$, collapse one after another.

Fig. 7(b) gives the mean value and standard deviation distributions. We can clearly identify that the bubbles appears in the middle region more frequently, according to the mean value distribution, while the most variation area of the bubbles lies in the periphery, as seen in the standard deviation distribution. Meanwhile one can find that this area is the place where the bubbles collapse, compared with Fig. 7(a). Since it is validated the bubble collapse site is the primary factor responsible for the cavitation erosion [28, 33], we assume that the standard deviation distribution based on the cavitation evolution structures can be applied for predicting the cavitation erosion area −the highest region stands for the most potential damaged area.

From the above analysis, one can find it is not a straightforward work to determine the cavitation evolution frequency, because the existence of the second cavitation clusters mentioned above. Hence, to obtain accurate data, a brightness detective method is applied on all the images by choosing a small monitor region (10×10 pixels) where most of the cavitation clouds collapse, as shown in Fig. 8. The selection of this monitor region can refer to the standard deviation distribution, since the highest value indicates the area where collapse happens. Accordingly, the cavitation frequencies are calculated by the mean of Power spectral density (PSD) analysis, based on the Fast Fourier transform (FFT) method.

Fig. 9 plots the results of PSD analysis under various cavitation numbers. In each graph, the highest amplitude value corresponds to the exact cavitation circulation frequency. It can

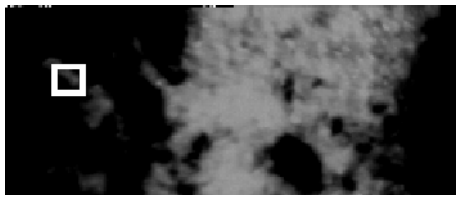

Fig. 8. Monitor window for FFT and PSD.

be noticed that as the cavitation number declines, the circulation frequency becomes much easier to distinguish from the PSD curve – the maximum amplitude is much clearly when σ bellows to 3.41. For higher cavitation numbers, the discrepancy of the amplitude against frequency turns less obvious. It is because the cavitation evolution, as mentioned above, is not that regular when σ is higher, contributing to sort of irregular circulation. Even though, the maximum amplitude can still be picked out easily. In general, one can find the cavitation circulation frequency decreases with the decreasing cavitation number, which means the cavitation circulation becomes longer, as shown in Fig. 10.

Fig. 11 shows the damaged aluminum foil after being exposed in cavitation for 5 min, at σ = 3.41. A ring-type eroded area can be seen directly by naked eyes. The diameter is approximately 40 mm, identical with the predicted standard deviation distribution in Fig. 5.

The cavitation erosion progress on the aluminum foil was recorded by high speed camera. We employed pit-count algorithm to detect the erosion pits [28, 38]. The images were also treated as matrices and post-processed in pairs – the image at the time t was subtracted from the image at time $t+\Delta t$, thus eliminating the surface and illumination imperfections and a new matrix was obtained, $Sub(i,j) = Image(i,j,t+\Delta t)-Image(i,j,t)$ (Fig. 12). Hence, from each image pair, the newly eroded pits number and damaged area were detected. However, since little vibration or illumination changes could cause differences between images, leading to changes in new matrix, a threshold parameter was applied to determine whether a certain variation is a pit or not. If the change exceeds the threshold, $Sub(i,j) = 1$, otherwise $Sub(i,j) = 0$. In the current work, the threshold is 25. Ultimately, we can obtain the accumulated pits distribution, the pits number and also eroded area. We could even determine the overlapping pits if $Sub(i,j) > 1$. Fig. 13 shows the recorded instantaneous raw images of aluminum foil in pairs and the post-processed images by pit-count algorithm, where the brighter area implies overlapping pits.

The chosen operation condition is σ = 3.41 and the time interval between each pair is $900\Delta t$, here Δt = 43.5 ms. The brighter area indicates the damaged pits, compared with the original image at $t = 0$. As seen from the experimental images, the pits are growing gradually in the region where cavitation collapses. Much clearer pits can be observed in the post-processed images, benefited from the pit-count algorithm, which eliminates the disturbances from illumination reflec-

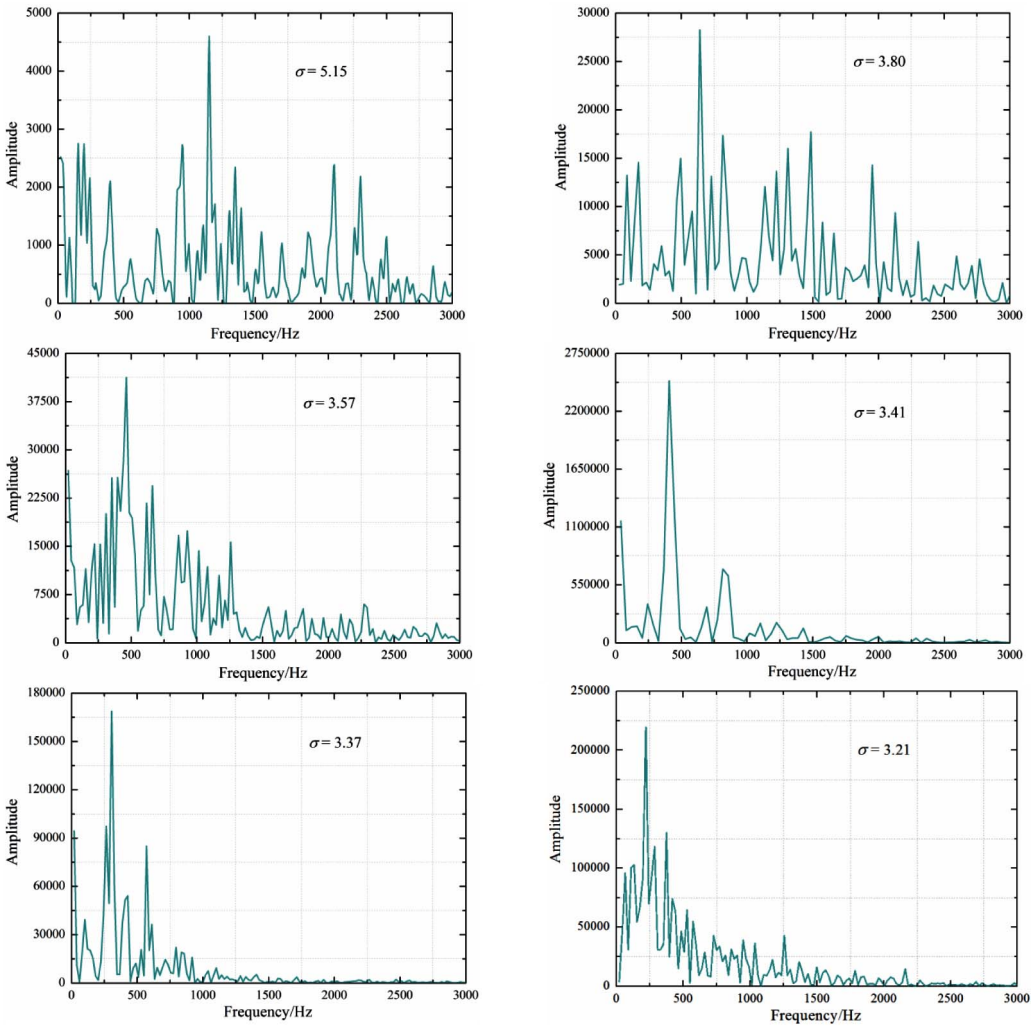

Fig. 9. PSD analysis on cavitation circulation frequency under various cavitation numbers.

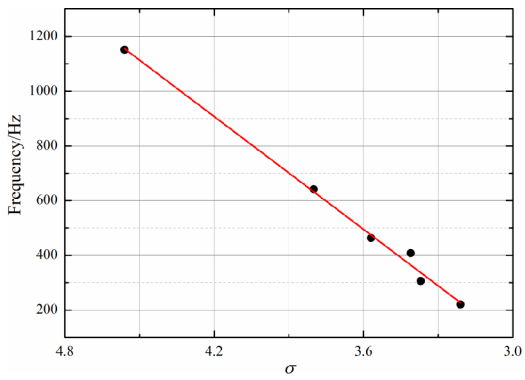

Fig. 10. Cavitation circulation frequency as a function of cavitation number.

tions or system vibration, resulting in more sharp contrast. One can see great agreement between experimental images and measured images. At the beginning of the exposure, the pits scatter nearby the collapse sites without many overlaps. However, since the cavitation tends to erode the place where

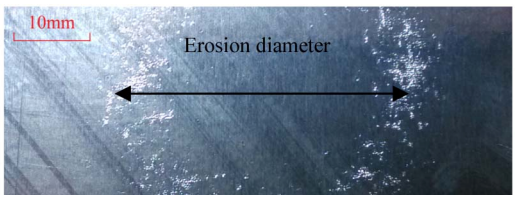

Fig. 11. Cavitation damaged aluminum foil at σ = 3.41.

has already been damaged or has surface defect [26], some of the erosion pits overlap each other consequently, giving rise to higher brightness after long exposure.

To investigate the cavitation intensity effect on erosion, two more tests were carried out by keeping the cavitation number constant as 3.41. Under this circumstance, the cavitation size remains unchanged, but the nozzle throat velocities are different. Based on the case in Fig. 13, where v = 12.9 m/s, the higher velocity condition was accomplished by increasing both the flow rate and upstream pressure, while the lower velocity was achieved in an opposite approach. The test results are given in Fig. 14. It is implied that the cavitation intensity

has profound impact on cavitation induced damage. We can see considerable distinction after enhancing the cavitation intensity – more damages are produced. Even so, the diameter of the eroded ring area nearly stays the same. On the contrary, reducing the cavitation intensity leads to lower damages and what's more, the damaged area is not annular.

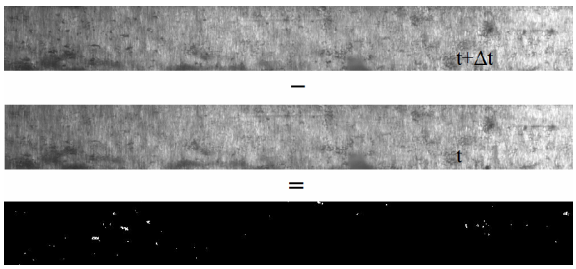

Fig. 12. Pit-count algorithm.

On the basis of the pit-count algorithm, the pits number accumulation as a function of time is obtained, as plotted in Fig. 15(a). It obviously indicates that the cavitation intensity significantly increase the damage process. The growth rate increases linearly with increasing velocity when keeping the cavitation number constant. To be more precise, we focus on a smaller time range from 43.5 s to 48.5 s. The case of v = 12.9 m/s is selected, as shown in Fig. 15(b). We can find that instead of a straightly linear pits increment, it presents a stepwise growth pattern. The reason lies in that the pits are mainly caused by the periodic cavitation collapse [28, 33], during the cavitation growing time, only a few pits could be generated.

4. Conclusions

In the current work, comprehensive cavitation evolution and cavitation induced erosion in orifice plate were experimentally

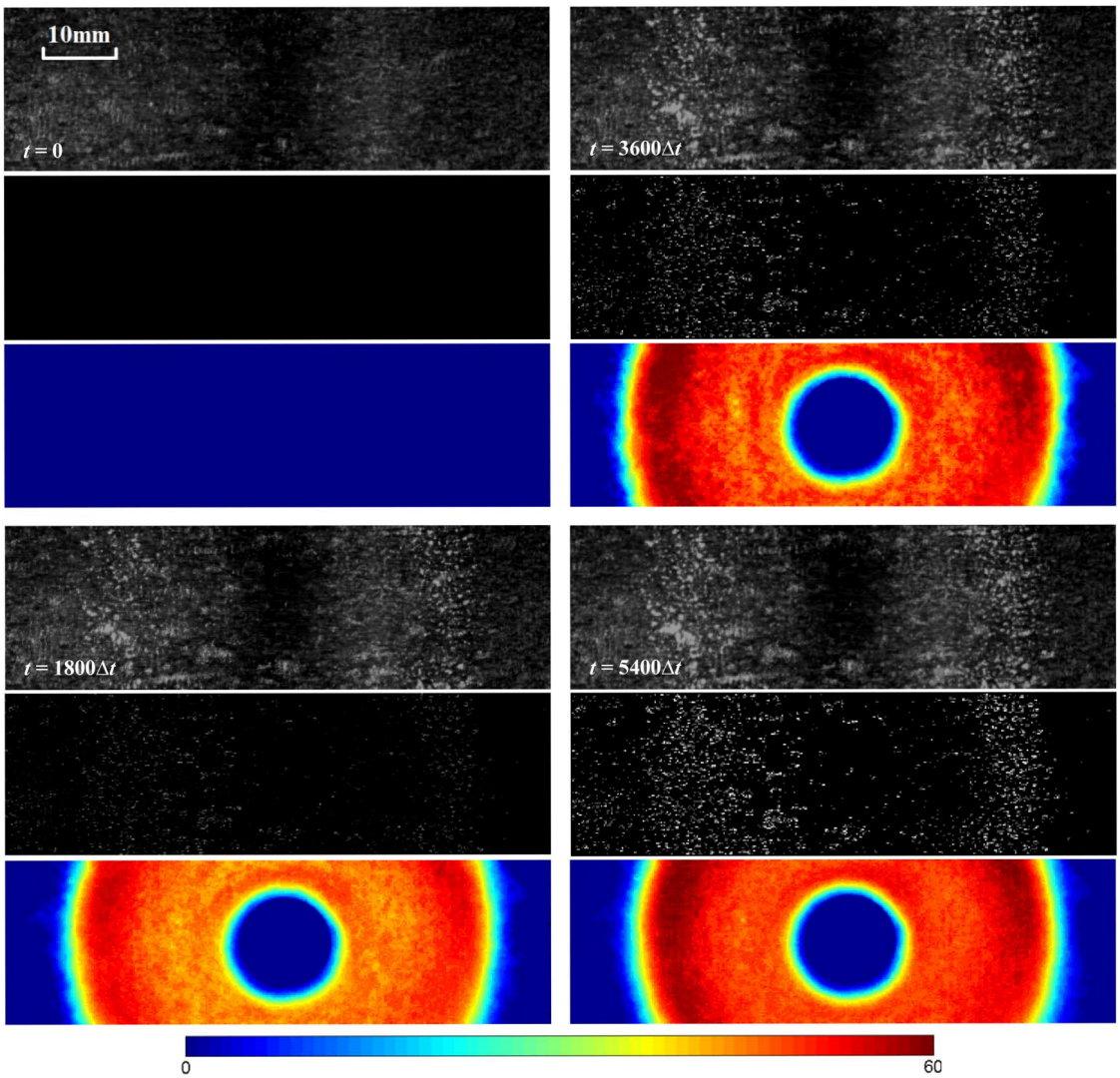

Fig. 13. Raw images of recorded aluminum foil (upper), post-processed images (middle) and predicted results of the eroded area at this instant (down) at σ = 3.41.

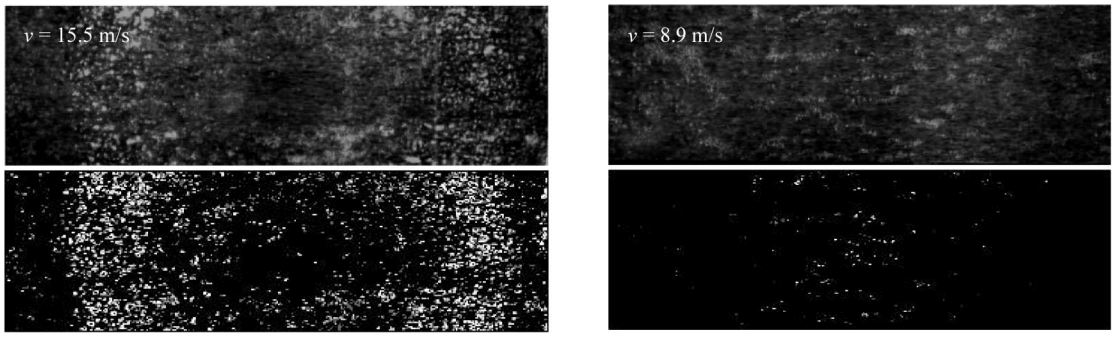

Fig. 14. Cavitation erosion tests under different velocity at constant cavitation number $\sigma = 3.41$.

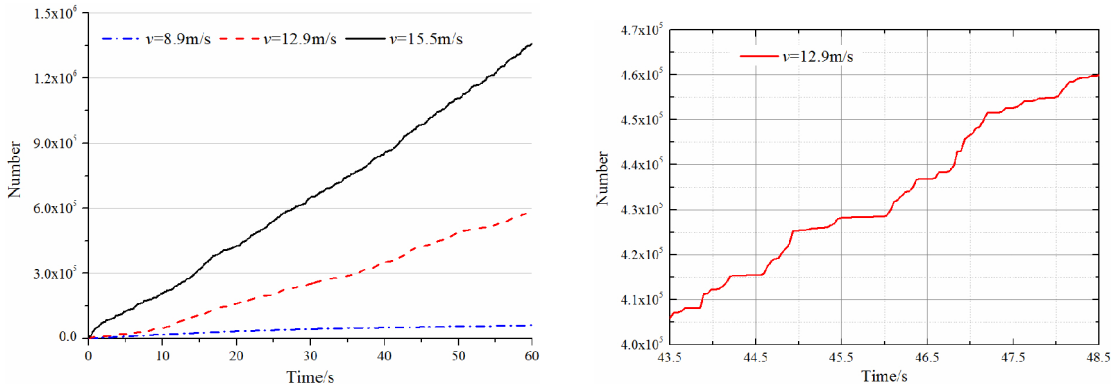

Fig. 15. Erosion pits number as a function a time: (a) 1 min; (b) 5 s.

investigated. Three image post-process methods were employed to analyze the results qualitatively and quantitatively. The conclusions can be drawn in several points:

(1) The cavitation structures were first studied. We see that the cavitation is in a form of circular ring and the diameter of it increases with declining cavitation number. Later, the first image post-process approach was applied to predict the potential cavitation erosion area by analyzing the instant cavitation evolution images. The results imply that the erosion area may cover almost all the cavitation developing route and the most vulnerable damaged area locates near the cavitation collapse sites.

(2) More precisely cavitation evolution was performed afterwards by focusing on a smaller region. It is found that even most of the cavitation clouds collapse at the rear part, there are still some tiny bubble clusters collapse as the cavitation moving downstream. Furthermore, when the attached cavitation sheds from the solid surface, some upstream bubble clusters stays still and shrinks gradually. Hence, it explains why the cavitation erosion area may cover the entire cavitation region. Additionally, we observed that in one circulation, there might be a second cavitation cloud following the first detached cloud, but it is not another cavitation inception. As a result, there could be three distinct cavitation clusters in one circulation.

(3) The Power spectral density analysis, based on the Fast Fourier transform approach (second post-processing approach), was adopted to calculate the cavitation evolution frequency. It is noticed that the PSD curves are more distinct while the cavitation number decreases, because the evolution process is more stable and fully developed. Meanwhile, the evolution frequency linearly reduces with decreasing cavitation number.

(4) Then, relying on the aluminum foil, the cavitation erosion tests were performed in a short duration. The pit-count algorithm (third approach) was applied to analyze the successive cavitation erosion images. Considerable agreement was observed compared with the predicted potential cavitation area, based on the standard deviation distribution – We see that the diameters of the predicted and experimental eroded ring are identical. Besides, by comparing with the erosion progress, it is validated that the pit-count algorithm is capable of giving a sound damage area.

(5) Ultimately, two more erosion tests were carried out under different flow velocities while keeping the cavitation invariable. It is find the cavitation intensity has strong effect on the erosion degree – The damages are enhanced when increasing the velocity, while in the contrast reducing the velocity leads to lower erosion aggressiveness. What's more, the eroded pits number growth curve against the time suggests that the damage increment pattern is stepwise instead of

straight linear.

Acknowledgements

The work was done in the scope of the is a part of a project "Cavitation in Thermosensible Fluids" financially supported by the European Space Agency (ESA). J. Wang would like to thank the State Scholorship Fund for the financial support by the China Scholarship Council which enabled him the stay at University of Ljubljana, during which this work was performed. And also, J. Wang would like to thank the support by the Research Foundation for Advanced Scholars of Taizhou University (Grant No.QD2013002); The National Natural Science Foundation of China (Grant No. 51609164, 51309120, 51239005); The Natural Science Foundation of Jiangsu Province (Grant No. BK20160574); The Jiangsu Industry University Research Cooperation Innovation Fund ─ forward joint research project (BY2015064-10); Priority Academic Program Development of Jiangsu Higher Education Institutions (PAPD); Open subject of Key Laboratory of Fluid and Power Machinery, Ministry of Education, Xihua University. (szjj2016-068), Jiangsu top six talent summit project (GDZB-017).

Nomenclature

n	: Number of images
p_∞	: Reference pressure
p_v	: Water saturation pressure
t, t_0	: Initial time
Δt	: Time interval
v	: Velocity
ζ	: Standard deviation
μ	: Mean value
ρ	: Water density
σ	: Cavitation number

References

[1] J. Wang, Y. Wang, H. L. Liu, H. Q. Huang and L. L. Jiang, An improved turbulence model for predicting unsteady cavitating flows in centrifugal pump, *International Journal of Numerical Methods for Heat & Fluid Flow*, 25 (2015) 1198-1213.

[2] H. L. Liu, J. Wang, Y. Wang, H. Q. Huang, H. Q. Huang and L. L. Jiang, Partially-averaged navier-stokes model for predicting cavitating flow in centrifugal pump, *Engineering Applications of Computational Fluid Mechanics*, 8 (2014) 319-329.

[3] Y. L. Wu, J. T. Liu, Y. K. Sun, S. H. Liu and Z.G. Zuo, Numerical analysis of flow in a Francis turbine on an equal critical cavitation coefficient line, *Journal of Mechanical Science and Technology*, 27 (6) (2013) 1635-1641.

[4] X. W. Luo, W. Wei, B. Ji, Z. B. Pan, W. C. Zhou and H. Y. Xu, Comparison of cavitation prediction for a centrifugal pump with or without volute casing, *Journal of Mechanical Science and Technology*, 27 (6) (2013) 1643-1648.

[5] B. Ji, X. Luo, Y. Wu, X. Peng and H. Xu, Partially-Averaged Navier–Stokes method with modified k–ε model for cavitating flow around a marine propeller in a non-uniform wake, *International Journal of Heat and Mass Transfer*, 55 (2012) 6582-6588.

[6] B. Ji, X. Luo, Y. Wu and K. Miyagawa, Numerical investigation of three-dimensional cavitation evolution and excited pressure fluctuations around a twisted hydrofoil, *Journal of Mechanical Science and Technology*, 28 (2014) 2659-2668.

[7] B. Y. Kang and S. H. Kang, Effect of the flat tank bottom on performance and cavitation characteristics of a cargo pump, *Journal of Mechanical Science and Technology*, 28 (2014) 3051-3057.

[8] X. M. Guo, L. H. Zhu, Z. C. Zhu, B. L. Cui and Y. Li, Numerical and experimental investigations on the cavitation characteristics of a high-speed centrifugal pump with a splitter-blade inducer, *Journal of Mechanical Science and Technology*, 29 (2015) 259-267.

[9] N. Pham-Thanh, H. Van Tho and Y. J. Yum, Evaluation of cavitation erosion of a propeller blade surface made of composite materials, *Journal of Mechanical Science and Technology*, 29 (2015) 1629-1636.

[10] L. Rayleigh VIII, On the pressure developed in a liquid during the collapse of a spherical cavity, *The London, Edinburgh, and Dublin Philosophical Magazine and Journal of Science*, 34 (1917) 94-98.

[11] Y. C. Wang and C. E. Brennen, *Shock wave development in the collapse of a cloud of bubbles*, ASME-American Society of Mechanical Engineers (1994) 15-19.

[12] J. E. Field, J. J. Camus, M. Tinguely, D. Obreschkow and M. Farhat, Cavitation in impacted drops and jets and the effect on erosion damage thresholds, *Wear*, 290 (2012) 154-160.

[13] J. P. Franc, M. Riondet, A. Karimi and G. L. Chahine, Impact load measurements in an erosive cavitating flow, *Journal of Fluids Engineering*, 133 (2011) 121301.

[14] D. Carnelli, A. Karimi and J. P. Franc, Application of spherical nanoindentation to determine the pressure of cavitation impacts from pitting tests, *Journal of Materials Research*, 27 (2011) 91-99.

[15] S. Hattori, T. Hirose and K. Sugiyama, Prediction method for cavitation erosion based on measurement of bubble collapse impact loads, *Wear*, 269 (2010) 507-514.

[16] H. Soyama, A. Lichtarowicz, T. Momma and E. J. Williams, A new calibration method for dynamically loaded transducers and its application to cavitation impact measurement, *Journal of Fluids Engineering*, 120 (1998) 712-718.

[17] R. T. Knapp, *Recent Investigations of the Mechanics of Cavitation and Cavitation Damage*, American Society of Mechanical Engineers (1954).

[18] R. T. Knapp, Accelerated field tests of cavitation intensity. *Transactions of the American Society of Mechanical Engineers*, 80 (1958) 91-102.

[19] B. Bachert, G. Ludwig, B. Stoffel, B. Sirok and M. Novak,

Experimental investigations concerning erosive aggressiveness of cavitation in a radial test pump with the aid of adhesive copper films, *Proceedings of the 5th International Symposium on Cavitation, CAV2003*, Japan (2003).

[20] E. Hutli, M. S. Nedeljkovic, A. Bonyár and D. Légrády, Experimental study on the influence of geometrical parameters on the cavitation erosion characteristics of high speed submerged jets, *Experimental Thermal and Fluid Science*, 80 (2017) 281-292.

[21] J. R. Laguna-Camacho, R. Lewis, M. Vite-Torres and J. V. Méndez-Méndez, A study of cavitation erosion on engineering materials, *Wear*, 301 (2013) 467-476.

[22] J. P. Franc, Incubation time and cavitation erosion rate of work-hardening materials, *Journal of Fluids Engineering*, 131 (2009) 021303.

[23] M. Rijsbergen, E. J. Foeth, P. Fitzsimmons and A. Boorsma, High-speed video observations and acoustic-impact measurements on a NACA 0015 foil, *Proceedings of the 8th International Symposium on Cavitation, CAV2012*, Singapore (2012).

[24] S. Lavigne, A. Retailleau and J. Woillez, Measurement of the aggressivity of erosive cavitating flows by a technique of pits analysis. Application to a method of prediction of erosion, *Proc. Int. Symp. Cavitation CAV95* (1995).

[25] X. Escaler, M. Farhat, F. Avellan and E. Egusquiza, Cavitation erosion tests on a 2d hydrofoil using surface-mounted obstacles, *Wear*, 254 (2003) 441-449.

[26] M. Dular and A. Osterman, Pit clustering in cavitation erosion, *Wear*, 265 (2008) 811-820.

[27] M. Dular, O. C. Delgosha and M. Petkovsek, Observations of cavitation erosion pit formation, *Ultrason Sonochem,* 20 (2013) 1113-1120.

[28] M. Petkovšek and M. Dular, Simultaneous observation of cavitation structures and cavitation erosion, *Wear*, 300 (2013) 55-64.

[29] G. Bark and R. E. Bensow, Hydrodynamic mechanisms controlling cavitation erosion, *International Shipbuilding Progress*, 60 (2013) 345-374.

[30]R. F. Patella, A. Archer and C. Flageul, Numerical and experimental investigations on cavitation erosion, *IOP Conference Series: Earth and Environmental Science*, 15 (2012).

[31] M. Dular, B. Stoffel and B. Širok, Development of a cavitation erosion model, *Wear*, 261 (2006) 642-655.

[32] N. Ochiai, Y. Iga, M. Nohmi and T. Ikohagi, Numerical prediction of cavitation erosion in cavitating flow, *Proceedings of the 7th International Symposium on Cavitation, CAV2009*, USA (2009).

[33] J. Wang, M. Petkovšek, H. L. Liu, B. Širok and M. Dular, Combined numerical and experimental investigation of the cavitation erosion process, *Journal of Fluids Engineering*, 137 (2015) 051302.

[34] Z. R. Li, M. Pourquie and T. van Terwisga, Assessment of cavitation erosion with a URANS method, *Journal of Fluids Engineering*, 136 (2014) 041101.

[35] M. Gavaises, F. Villa, P. Koukouvinis, M. Marengo and J.-P. Franc, Visualisation and les simulation of cavitation cloud formation and collapse in an axisymmetric geometry, *International Journal of Multiphase Flow*, 68 (2015) 14-26.

[36] F. Brand, Ein physikalisches verfahren zur bestimmung von geloesten und ungeloesten gasen in wasser, *Voith Forschung und Konstruktion*, 27 (1981).

[37] M. Dular, B. Bachert, B. Stoffel and B. Širok, Relationship between cavitation structures and cavitation damage, *Wear*, 257 (2004) 1176-1184.

[38] T. Keil, P. F. Pelz, U. Cordes and G. Ludwig, Cloud cavitation and cavitation erosion in convergent divergent nozzle, *WIMRC 3rd International Cavitation Forum 2011*, University of Warwick, UK (2011) 1-7.

J. Wang received his Ph.D. degree from Research Center of Fluid Machinery Engineering and Technology, Jiangsu University in 2015. He has been engaged in cavitating flows and cavitation erosion in hydrodynamic machines.